

Appendix

Part I Introduction of Camellia Fruit Picking Background Technology

1、 The same period of flowers and fruits

Camellia fruit has the characteristics of the growth of the same period of flower and fruit, that is, when the Camellia fruit matures in the same year, the flowers that bear fruit in the second year open at the same time.



Figure 1. camellia tree with fruits and flowers

2、 Brief introduction to the research of Camellia fruit picking machine of our team

The push-shake camellia fruit picking machine is a forest fruit vibration picking robot designed by our research group that can realize the automatic picking of camellia fruit. The biggest difference between this picking machine and the electric camellia fruit picking robot we designed in 2015 is that it adopts the design of mechatronic and hydraulic integration. In 2015, we designed China's first camellia fruit picking robot. The main problem is that the use of servo motors produces large vibration power consumption, high cost, small amplitude and low picking efficiency. The economic cost and the result of the experiment made us deny the original plan, and the hydraulic system was added to reduce the size of the picking

robot and improve the vibration output capability of the picking robot. The picking robot designed in 2015 is shown in Figure 2(a), and the latest designed picking robot is presented in Figure 2(b).

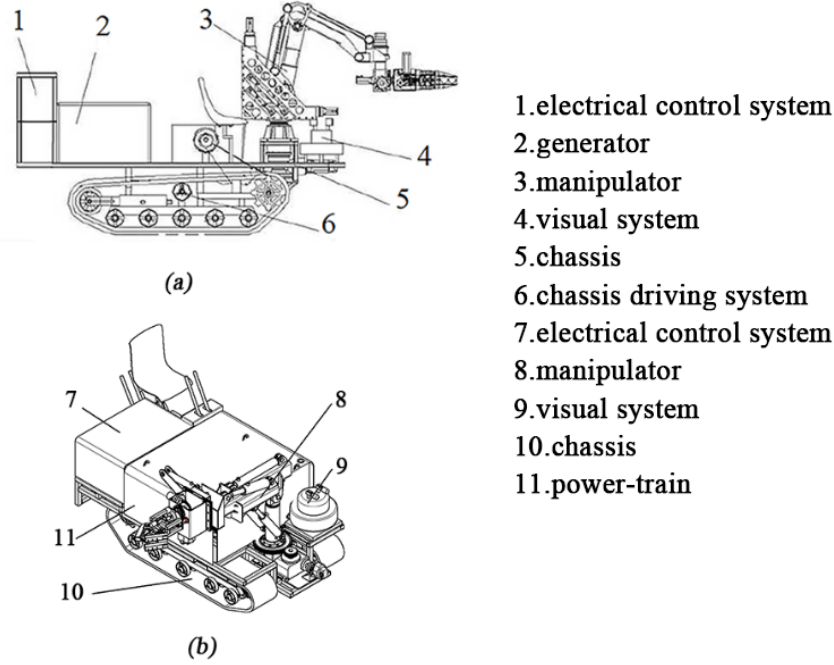


Figure 2. camellia fruit picking robot

Part II Supplementary description of the mathematical model of the plant

3、 Force analysis diagram of hydraulic motor shaft

The hydraulic motor shaft is in a balanced state by the interaction of five torques, namely hydraulic driving torque $\frac{V_{stm}\Delta p_m}{2\pi}$, inertial torque $J_t \frac{d^2\Delta\theta_m}{dt^2}$, viscous resistance torque $c_m \frac{d\Delta\theta_m}{dt}$, elastic torque $G\Delta\theta_m$ and load reaction torque ΔT under stable conditions. Therefore, the following formula can be obtained from the force balance relationship:

$$\frac{V_{stm}\Delta p_m}{2\pi} = J_t \frac{d^2\Delta\theta_m}{dt^2} + c_m \frac{d\Delta\theta_m}{dt} + G\Delta\theta_m + \Delta T$$

where:

J_t —— total momentum of inertia on hydraulic motor shaft(including loads)

c_m —— viscous damping coefficients of hydraulic motors and loads

G —— torsional stiffness of loads

T — load torque on hydraulic motor shaft

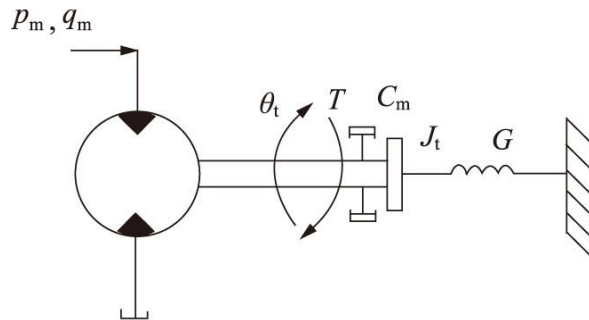


Figure 3. force analysis diagram of hydraulic motor

4、 Supplementary description of the control element of the pilot-operated electro-hydraulic proportional flow valve

An active pilot electro-hydraulic proportional flow valve is mentioned on pages 9-10 of the article, and its basic working principle is described as follows:

The control system can control the speed of the DC motor by controlling the voltage. The DC motor is the component that drives the small bidirectional hydraulic pump, and the flow of the pilot valve installed at the outlet of the hydraulic pump can be adjusted by controlling its forward and reverse rotation. The flow of the pilot valve is proportional to the flow of the main valve, thus realizing the control of the vibration hydraulic motor connected to the main valve.

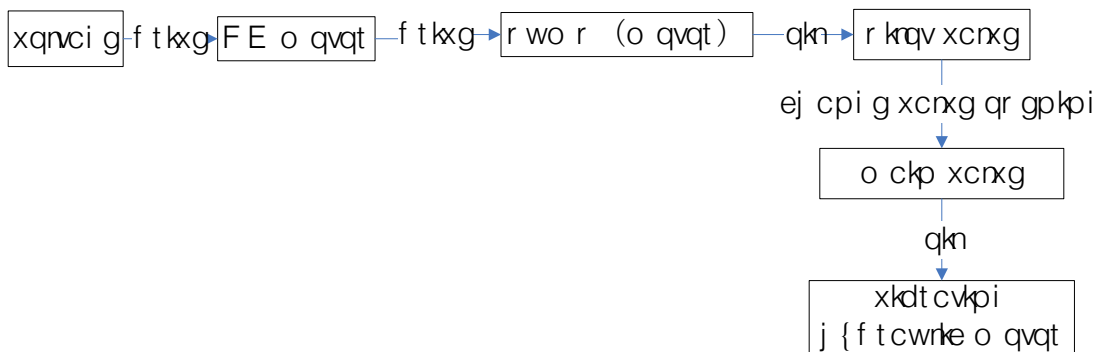


Figure 4. working principle diagram of the electro-hydraulic proportional flow valve

The drive circuit of the pilot valve DC motor can be simplified as the circuit diagram shown in Figure 5. Therefore, according to Kirchoff's law in the above circuit, the formula is obtained:

$$\Delta U_f = R\Delta i + L \frac{d\Delta i}{dt} + C_e \Delta \omega_0$$

where:

U_f — armature voltage on the DC motor

R — resistance of the load

- i — loop current
- L — inductance of the load
- C_e — back EMF coefficient
- ω_0 — angular velocity of motor

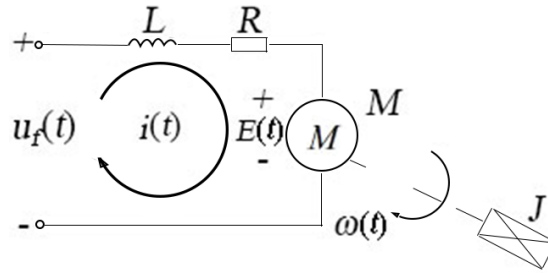


Figure 5. Pilot valve DC motor drive circuit

Part III Stability Analysis of Controlled System

5、Stability analysis of the system

The transfer function matrix of the system is derived by the following procedure. The state space equation of the system is:

$$\begin{cases} \dot{x} = Ax + Bu \\ y = Cx \end{cases} \quad (1)$$

The Laplace transform is taken on the above equation and the equation becomes:

$$\begin{cases} sX(s) - X(0) = AX(s) + BU(s) \\ Y(s) = CX(s) \end{cases} \quad (2)$$

Where: $X(0)$ represents the value of $X(t)$ at the initial time $t=0$.

Since the transfer function describes the relationship between the input and output of the system, the influence of the system on the initial conditions can be ignored. So take $X(0)=0$. Then the above equation becomes:

$$\begin{cases} X(s) = (sI - A)^{-1} BU(s) \\ Y(s) = CX(s) \end{cases} \quad (3)$$

Where: I represents the identity matrix.

Therefore, the transfer function matrix of the system can be obtained as:

$$G(s) = \frac{Y(s)}{U(s)} = C(sI - A)^{-1} B \quad (4)$$

The above equation (4) is used to calculate the transfer function matrix of the

system, and draw its Nyquist diagrams and bode diagrams as shown in the following Figure 6.

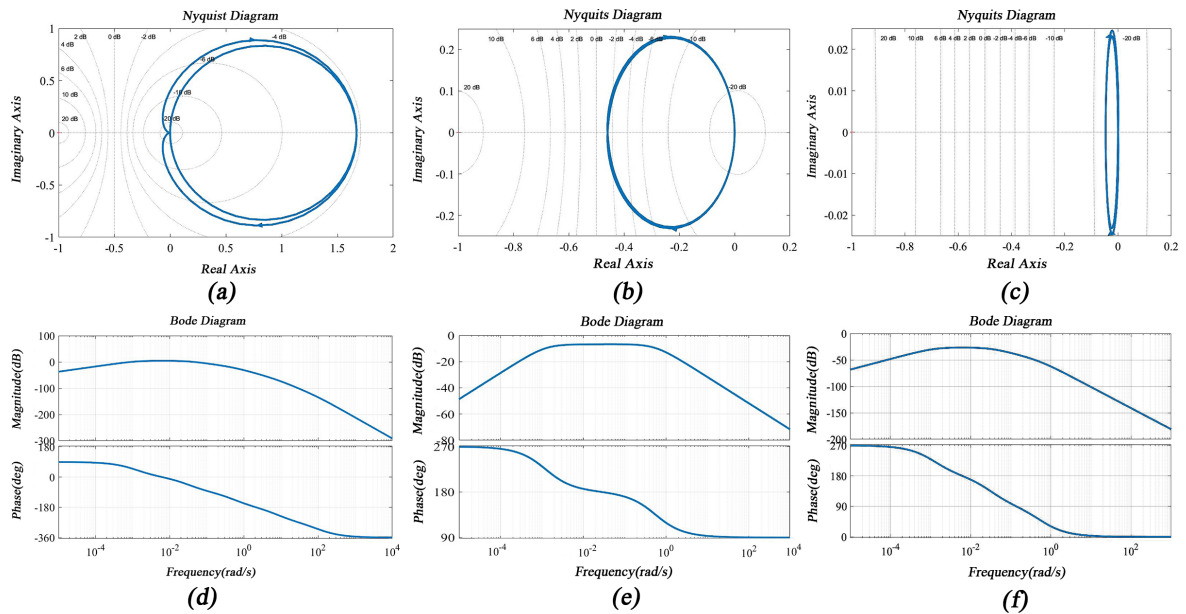


Figure 6. Nyquist and bode diagrams of the system

The Nyquist and bode plots of the transfer function G_{11} between Y and input U_1 are shown in Fig. 6(a) and (d). The number of open-loop poles on the right side of the system is $P=0$ and $R=0$, so the number of closed-loop poles on the right side of the s -plane $Z=P-R=0$, the system is stable. Where R is the number of clockwise turns of the open-loop system $G(s)H(s)$ around the point $(-1, j_0)$. The Nyquist and bode plots of the transfer function G_{12} between Y and input U_2 are shown in Fig. 6(b) and (e). The $P=0$ and $R=0$, so the $Z=P-R=0$, the system is stable. The Nyquist and bode plots of the transfer function G_{13} between Y and input U_3 are shown in Fig. 6(c) and (f). The $P=0$ and $R=0$, so the $Z=P-R=0$, the system is stable.

In summary, according to the Nyquist stability criterion, the whole system is in a stable state, and it can be seen from the bode diagram that only the amplitude margin and phase margin of G_{11} are limited, which needs to be adjusted by regulating the three parameters of the PID controller.

Part IV Simulation setting and analysis in MATLAB/Simulink and field test

6、Establishment of PID Controller

PID (Proportional Integral Derivative) control originated in the late 1930s and is still widely used today. It is widely used in industrial process control and agricultural engineering due to its simple algorithm, good robustness and high reliability. PID control method can actually solve the control problem of the system, of which structure and parameters cannot be completely determined or the mathematical model cannot be completely accurate, very well.

The basic principle of PID control is to control the deviation $\varepsilon(t)$ through

proportional, integral and differential transformations. The basic control law is:

$$u(t) = K_p \left[\varepsilon(t) + \frac{1}{T_i} \int_0^t \varepsilon(\tau) d\tau + T_d \frac{d\varepsilon(t)}{dt} \right]$$

where:

- K_p — proportional coefficient
- T_i — integral time
- T_d — differential time

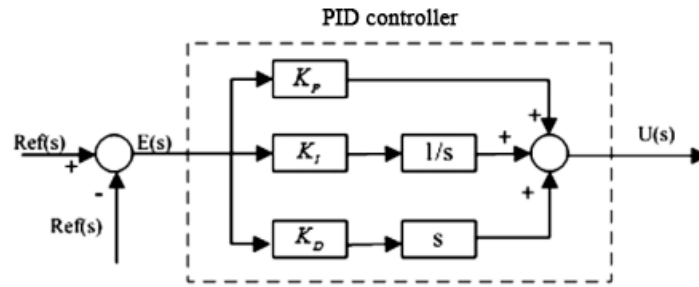


Figure 7. PID Controller

Incremental digital PID controller is a digital PID that uses the increment of the input as the control variable. It can be controlled by computer programming and it has the characteristics of strong flexibility and high programmability. It is widely used in the control of electromechanical products. Its control law is:

$$\begin{aligned} \Delta u(k) &= u(k) - u(k-1) \\ &= K_p [e(k) - e(k-1)] + K_i e(k) + K_D [e(k) - 2e(k-1) + e(k-2)] \end{aligned}$$

In the formula: $u(k)$ and $u(k-1)$ are the k th and $k-1$ th output values of the controller; K_p is the proportional coefficient; K_i is the integral coefficient; K_D is the differential coefficient; $e(k)$, $e(k-1)$ and $e(k-2)$ are the k th, $k-1$ th, and $k-2$ th input error values.

The digital PID controller can flexibly adjust the three parameter values of proportional K_p , integral K_i and differential K_D through the software or operation logic of the computer or microcontroller, so as to realize the control of the controlled object. This control method only needs to sample the deviation results of the current sample time and its latest two sample time to realize programming control. This control method is used to the operation of our first camellia fruit picking robot (Gao et al., 2019). Therefore, PID controller is also used to control its picking operation in the control of our second-generation camellia fruit picking robot. The PID control simulation model built according to the controlled object is shown in Figures 8-9.

control rules, the three parameters K_P , K_I and K_D of PID are optimized and adjusted in real time, and the real-time automatic adjustment of PID controller is realized. As shown in Figure 10.

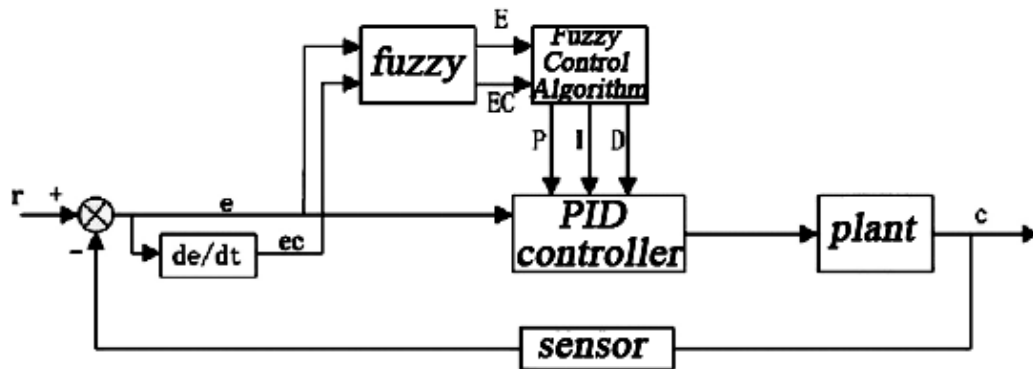


Figure 10. Fuzzy PID controller

The working principle of the fuzzy PID controller is to detect the real-time output parameters of the controlled object through sensors and compare them with the given values to obtain the error e , and obtain the error rate of change ec through differential operation, and use them as two-dimensional fuzzy control. According to the input of the controller, the fuzzy inference engine outputs the adjusted three parameter values of K_P , K_I and K_D to the PID controller according to the fuzzy control rules, so as to realize the real-time adjustment of the parameters of the PID controller. In this project, we select the membership function images of the input and output of the fuzzy system as shown in Figure 11 and Figure 12 below. A faster response is required to adjust the whole system, so a Gaussian membership function is used at both ends due to the large error at both ends. The error in the middle is small, and fine-tuning of the parameters is required, so the triangular membership function is used in the middle. The fuzzy inference rules were set according to experience (Han et al., 2022), as shown in Table 2 below.

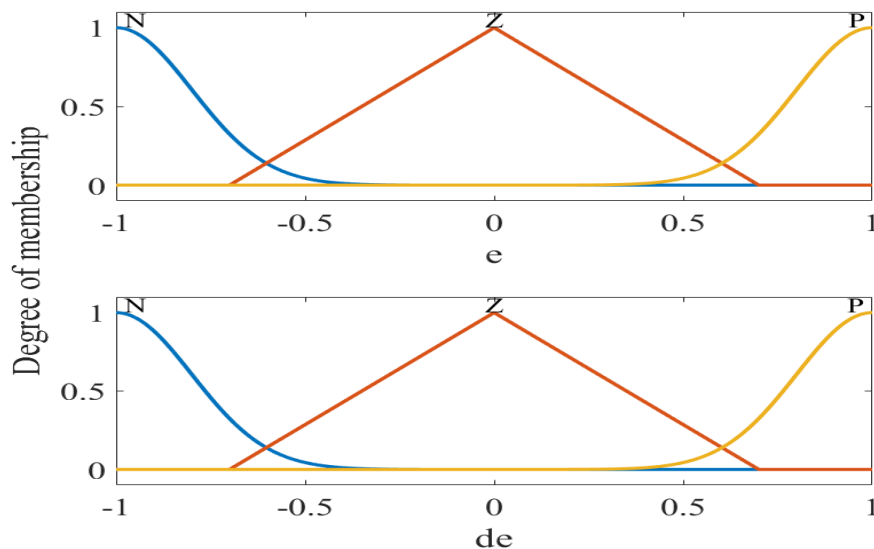


Figure 11. Input membership function

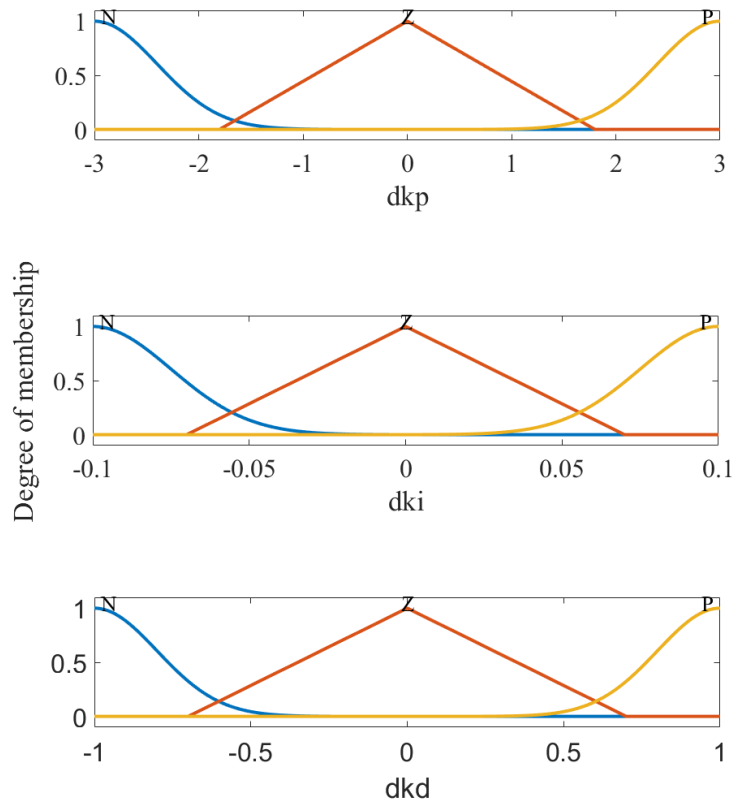


Figure 12. Output membership function

Table 2. Fuzzy Rule Table

de	e		
	N	Z	P
N	(P,N,P)	(P,N,N)	(Z,Z,P)
Z	(P,N,Z)	(Z,Z,N)	(N,P,Z)
P	(Z,Z,P)	(N,Z,P)	(N,P,P)

The FPID controller module in the MATLAB/Simulink is shown in Figure 13-15.

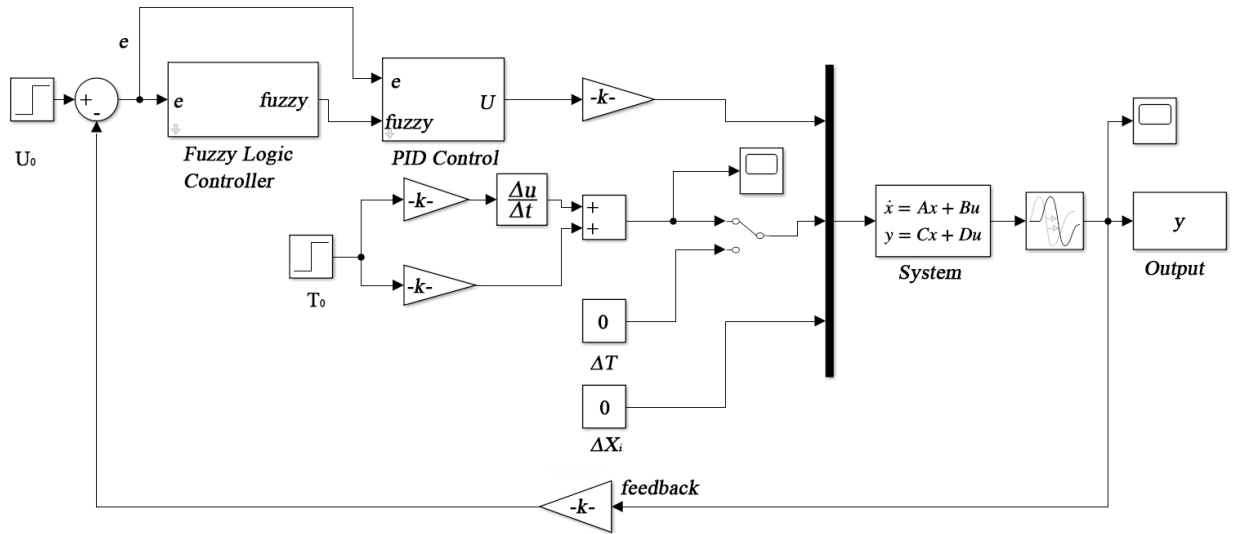


Figure 13. Fuzzy PID controller simulation model

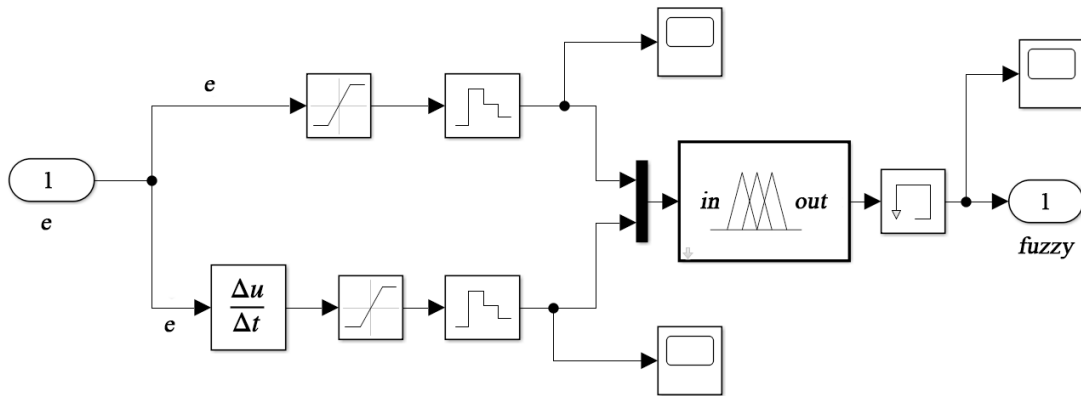


Figure 14. Fuzzy Logic Controller Simulation sub-module

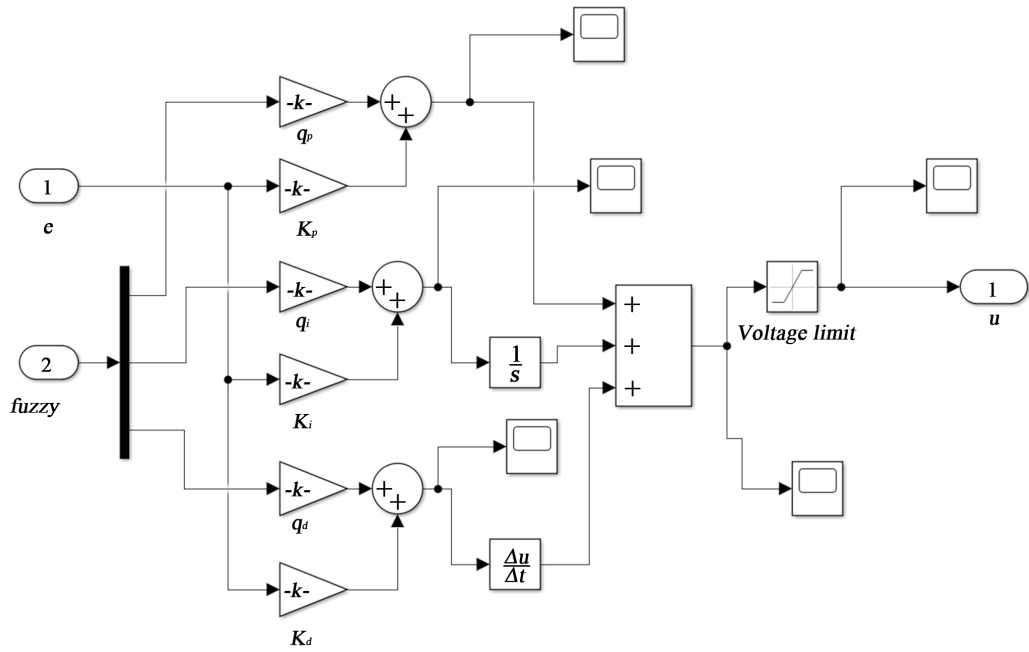


Figure 15. PID controller simulation sub-module

8、Establishment of FNN PID Controller

(1) FWNN

The MATLAB/Simulink simulation module of the fuzzy wavelet neural network PID controller designed in the article is shown in Figure 16-18.

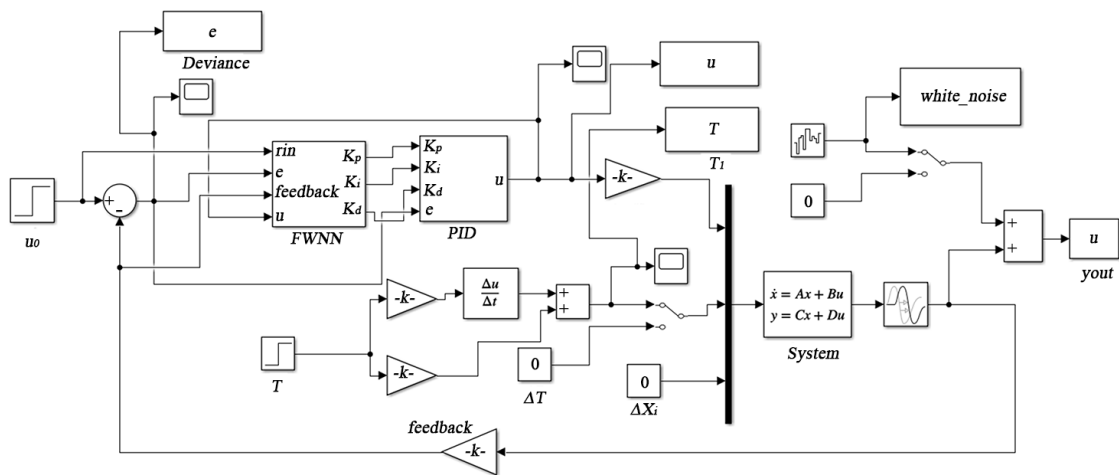


Figure 16. FWNN PID controller designed in Simulink

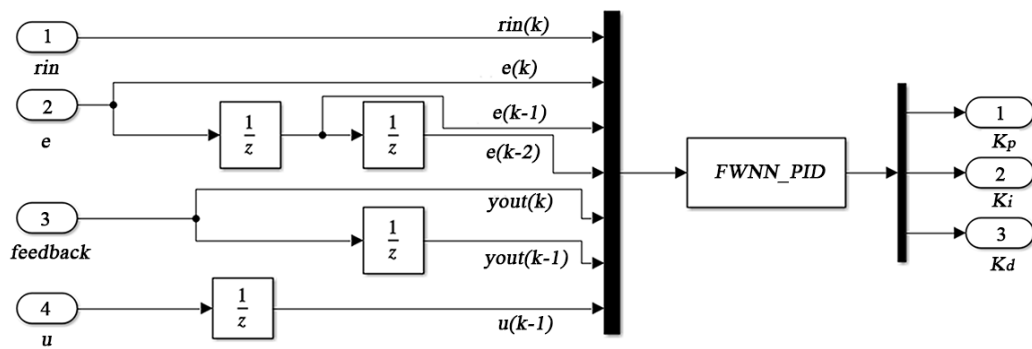


Figure 17. FWNN simulation module

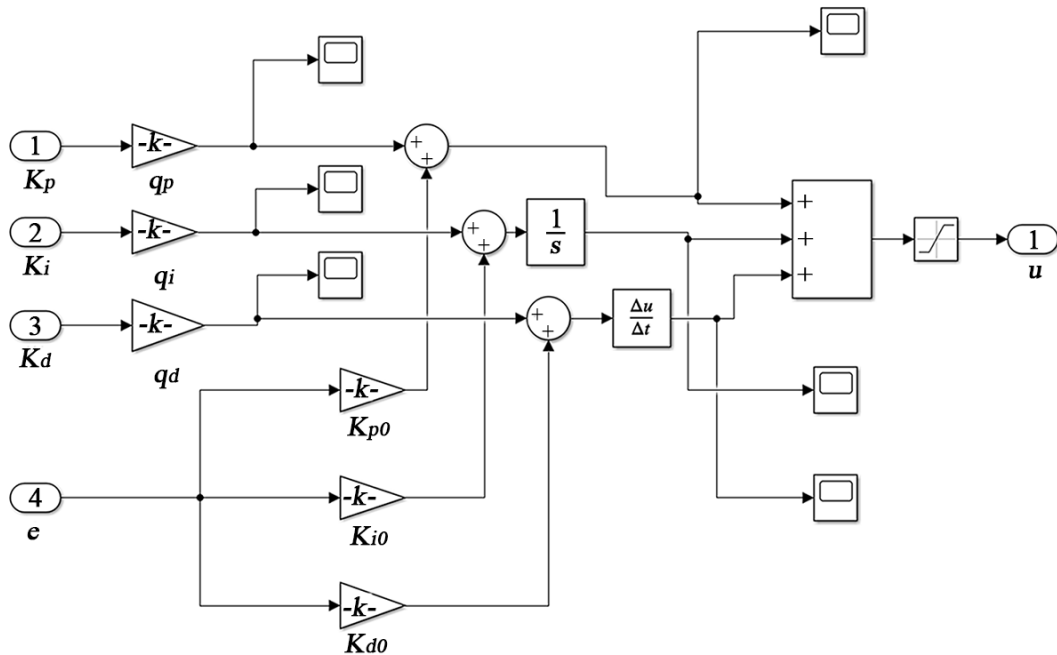


Figure 18. PID simulation module

(2) FRBFNN

Fuzzy neural network is an ingenious combination of fuzzy control system and neural network, giving full play to the advantages of both. Its essence is to give the neural network fuzzy input signals and weights on the basis that the neural network learning algorithm is unchanged or improved. FRBF neural network is a neural network formed by combining fuzzy control system with RBF neural network.

The topology of the fuzzy RBF neural network designed in this paper is shown in Figure 17, which is a four-layer $A-2B-B^2-C$ network structure, and the four layers are the input layer, the fuzzification layer, the fuzzy inference layer and the output layer.

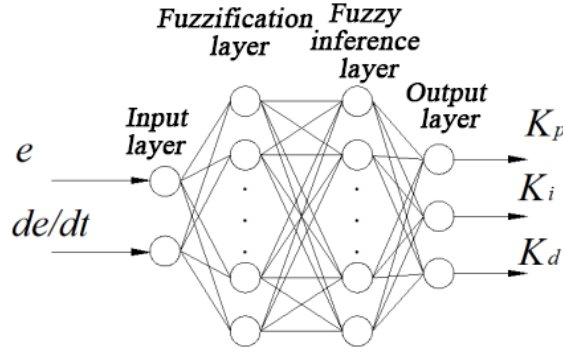


Figure 19. Fuzzy RBF neural network

1) Input layer: The function of this layer is to obtain the network input and pass it to the next layer. The mathematical expression of the input of each node i is:

$$f_1(i) = X_i$$

2) Fuzzification layer: The function of this layer is to fuzzify the input variables, the number of nodes is equal to the sum of the number of subsets of the fuzzification amount of the input variables, and also has the function of calculating the membership function of the input variables. The membership function used by the RBF neural network is the Gaussian basis function, so the calculation formula of the second layer is:

$$f_2(i, j) = \exp\left(-\frac{(f_1(x_i) - c_{ij})^2}{(b_j)^2}\right)$$

3) Fuzzy inference layer: This layer is connected to the fuzzification layer, and the fuzzified input is inferred based on the fuzzy rule table, that is, the respective ignition intensity is obtained according to the node matching relationship. The calculation formula is:

$$f_3(j) = \prod_{j=1}^N f_2(i, j)$$

The fuzzy rule table designed in this paper for matching between the fuzzification layer and the fuzzy inference layer is shown in Table 3 below.

Table 3. Fuzzy rule table of ΔK_P , ΔK_I , ΔK_D

	e_c	e						
		<i>NB</i>	<i>NM</i>	<i>NS</i>	<i>ZO</i>	<i>PS</i>	<i>PM</i>	<i>PB</i>
ΔK_P	<i>NB</i>	<i>PB</i>	<i>PB</i>	<i>PM</i>	<i>PM</i>	<i>PS</i>	<i>ZO</i>	<i>ZO</i>
	<i>NM</i>	<i>PB</i>	<i>PB</i>	<i>PM</i>	<i>PS</i>	<i>PS</i>	<i>ZO</i>	<i>NS</i>
	<i>NS</i>	<i>PM</i>	<i>PM</i>	<i>PM</i>	<i>PS</i>	<i>ZO</i>	<i>NS</i>	<i>NS</i>
	<i>ZO</i>	<i>PM</i>	<i>PM</i>	<i>PS</i>	<i>ZO</i>	<i>NS</i>	<i>NM</i>	<i>NM</i>
	<i>PS</i>	<i>PS</i>	<i>PS</i>	<i>ZO</i>	<i>NS</i>	<i>NS</i>	<i>NM</i>	<i>NM</i>
	<i>PM</i>	<i>PS</i>	<i>ZO</i>	<i>NS</i>	<i>NM</i>	<i>NM</i>	<i>NM</i>	<i>NB</i>
	<i>PB</i>	<i>ZO</i>	<i>NS</i>	<i>NM</i>	<i>NM</i>	<i>NM</i>	<i>NB</i>	<i>NB</i>

ΔK_I	NB	NB	NB	NM	NM	NS	ZO	ZO
	NM	NB	NB	NM	NS	NS	ZO	ZO
	NS	NB	NM	NS	NS	ZO	ZO	ZO
	ZO	NM	NM	NS	ZO	PS	PM	PM
	PS	NM	NS	ZO	PS	PS	PM	PM
	PM	ZO	ZO	PS	PS	PM	PB	PB
	PB	ZO	ZO	PS	PM	PM	PB	PB
ΔK_D	NB	PS	NS	NB	NB	NM	NM	PS
	NM	PS	NS	NM	NM	NM	NS	ZO
	NS	ZO	NS	NM	NM	NS	NS	ZO
	ZO	ZO	NS	NS	NS	NS	NS	ZO
	PS	ZO						
	PM	PB	NS	PS	PS	PS	PS	PB
	PB	PB	PM	PM	PM	PS	PS	PB

4) Output layer: The function of this layer is to output based on the fuzzy rules and the inference conclusion of the fuzzy inference layer. The calculation formula is:

$$f_4(i) = w \bullet f_3 = \sum_{j=1}^N w(i, j) \bullet f_3(j)$$

where:

w — connection weight matrix between the fuzzy inference layer and the output layer

The weight adjustment method used by the FRBF neural network is the same as the fuzzy wavelet neural network, which is the gradient descent method, that is, the content described on pages 19 to 20 of the main text.

The above FRBF neural network PID controller built in MATLAB/Simulink in the simulation of the paper is shown in Fig. 20-22 below.

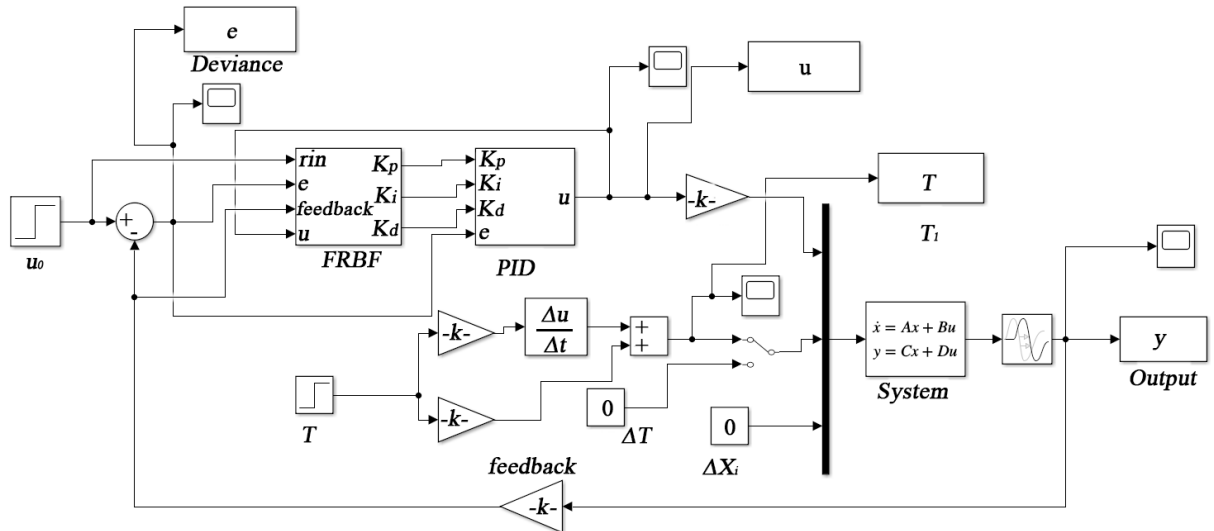


Figure 20. Fuzzy neural network PID simulation module

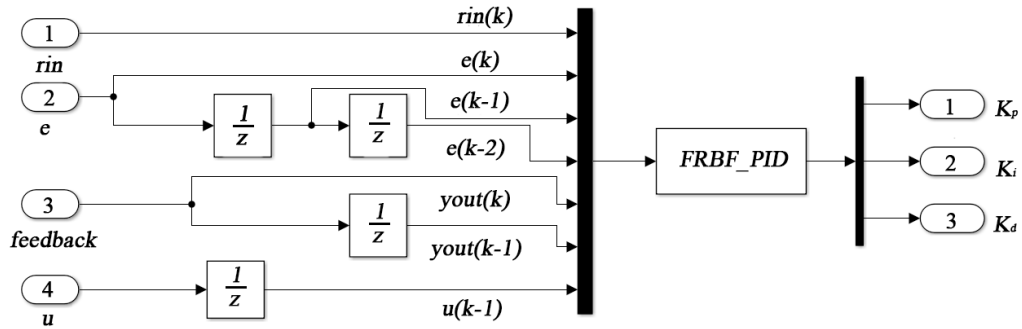


Figure 21. Fuzzy RBF neural network simulation sub-module

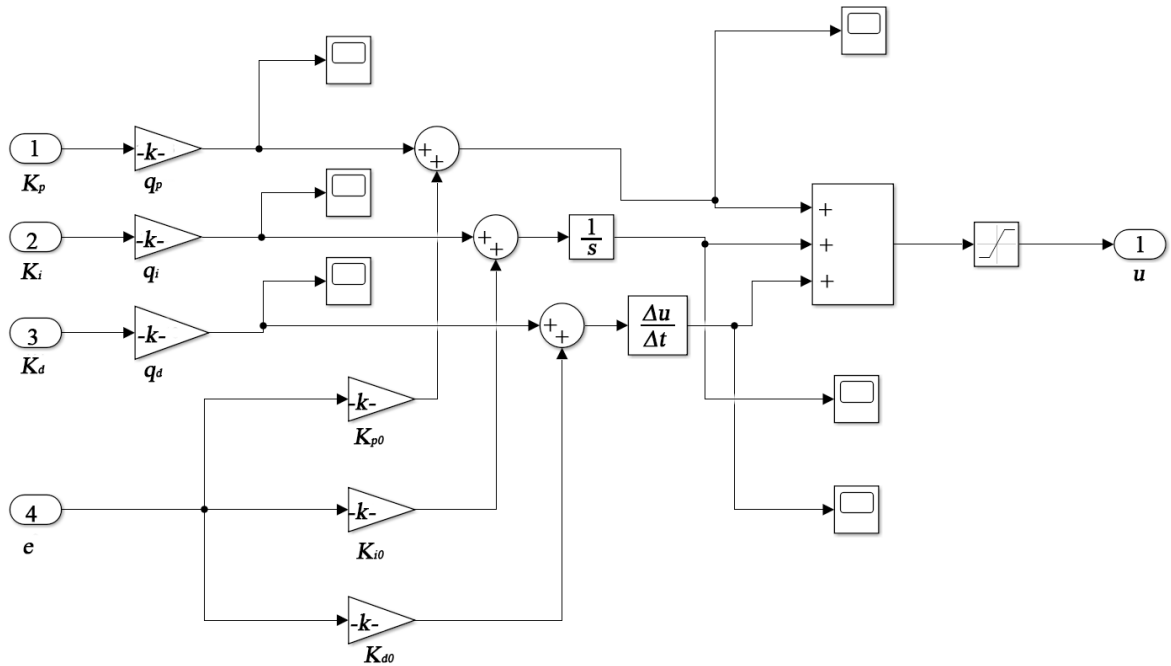


Figure 22. Adaptive PID controller simulation sub-module

9、Simulation parameter setting in the system

The simulation-related parameters used in the simulation of the paper and the set external interference are shown in Fig.23 and Table 4~6 below. The relevant parameters of the hydraulic system and electronic control system involved in the simulation are all taken from the relevant parameters given by the outsourcing manufacturer of the picking machine in this project.

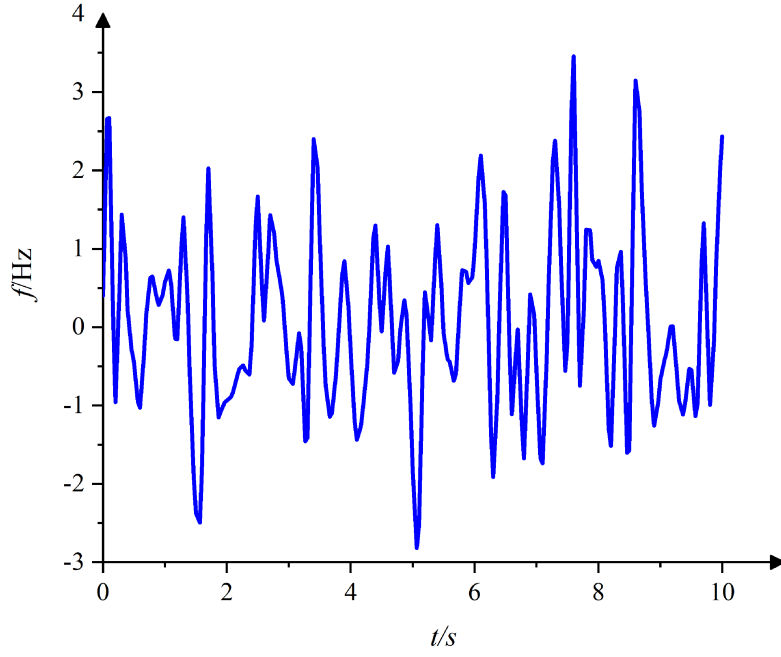


Figure 23. white noise input in simulation

Table 4. Simulation parameter list

DC motor		Electro-hydraulic proportional flow valve		Vibrating hydraulic motor	
R	9.5Ω	k_{xb}	12.087	V_{stm}	58.4ml/r
C_M	$0.284V \cdot s \cdot rad^{-1}$	k_w	9952.2ml/min	K_{cm}	1.2
	0.088H				
L		k_m	$0.0267ml \cdot s^{-1} \cdot MPa$	V_m	25.68ml
C_e	$0.029N \cdot m \cdot A^{-1}$	k_{qF}	1330ml/mm	E_m	0.7GPa
J	$1.6 \times 10^{-4} kg \cdot m^2$			J_t	60750kg·mm ²
B	$3.82 \times 10^{-4} N \cdot m \cdot s \cdot rad^{-1}$			c_m	600N·mm/deg
				G	2480N·mm·deg

Table 5. Parameters of FRBF

η	α
0.2	0.05

Table 6. Parameters of FWNN

η	α	d	t
0.2	0.05	0.2	0.05

10、Influence analysis of the pre-opening increment of feedback throttle slot

The pre-opening increment of the feedback throttling slot is related to the initial

state of the valve. Once the valve is in operation, it will be a fixed value. In order to study its influence on the control system, the simulation module shown in Figure 9 is built in MATLAB/Simulink. The pre-opening of the valve port expresses the opening degree of the valve port in the initial state, which is usually expressed as a percentage in mathematics. Since the value range of the valve port pre-opening is [0,1], the pre-opening was set to 0, 0.5 and 1 in the simulation, and the research was carried out under no-load conditions. The simulation environment is exactly the same as the article text system environment, and the simulation time is still set to 10s. The simulation results are shown in Fig.25.

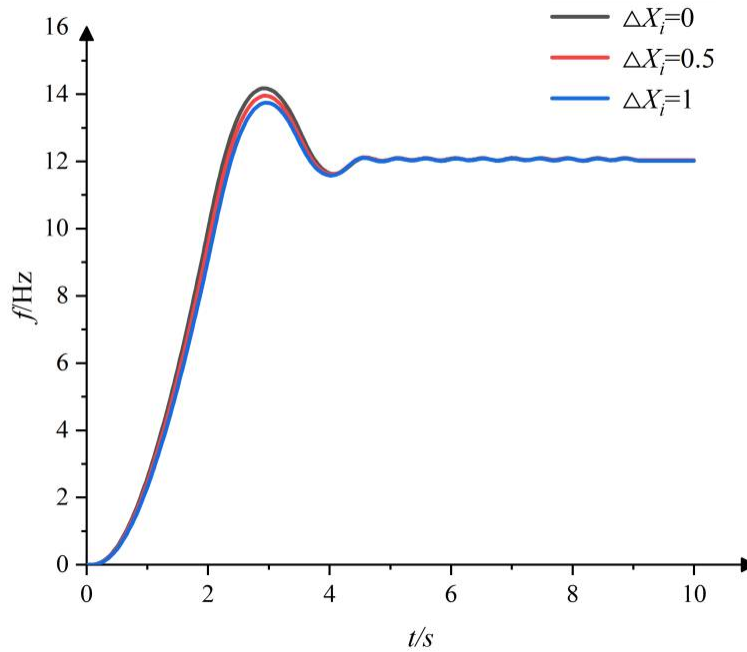


Figure 25. Influence of feedback throttle slot valve port pre-opening on System

Table 7. Parameters of maximum overshoot

pre-opening degree	$\Delta X_i=0$	$\Delta X_i=0.5$	$\Delta X_i=1$
Maximum overshoot	17.7%	16.1%	14.3%

It can be seen from the above simulation results that under no-load conditions, the larger the valve port pre-opening, the smaller the overshoot. However, even if the degree of the pre-opening reaches the maximum, the difference between the maximum overshoot of the degree of the maximum and the minimum is not more than 3.4%, so this factor has little influence on the entire system. Therefore, the pre-opening degree was set to 0, that is, the situation where the pre-opening of the valve port has the greatest influence on the overshoot in the subsequent simulation, in order to verify the influence of other factors on the system.

11、 Display of the field test measurement results data

During the field test, the 1200mm thick branches of the same variety of *Camellia oleifera* trees were picked respectively. Each group of 9 trees was set at three different frequencies of 12Hz, 15Hz and 18Hz to generate excitation. A total of 27 groups of 243 *Camellia oleifera* trees were picked. The experimental data are shown in Tables

8-10 below, and the experimental comparison results and conclusions are shown on pages 28-29 of the main text.

Table 8. picking test results of PID controller

The number of test groups	Excitation frequency/Hz	Average picking time/s	Average rate of dropping flowers/%	Average rate of dropping fruits/%
1	12	146	8.9	86.2
2	12	138	9.7	83.6
3	12	137	10.8	87.4
4	15	129	8.6	80.2
5	15	123	7.8	76.8
6	15	119	8.3	81.9
7	18	106	11.2	86.7
8	18	112	12.9	87.3
9	18	114	11.8	84.7
Average		124.8	10.0	83.9

Table 9. picking test results of FRBFNN PID controller

The number of test groups	Excitation frequency/Hz	Average picking time/s	Average rate of dropping flowers/%	Average rate of dropping fruits/%
10	12	98	5.6	88.4
11	12	102	3.2	90.6
12	12	106	4.8	91.2
13	15	96	7.4	86.5

14	15	101	4.9	88.7
15	15	97	8.4	93.4
16	18	94	9.5	91.7
17	18	92	7.8	95.6
18	18	95	9.8	91.8
Average		97.9	6.8	90.9

Table 10. picking test results of FWNN PID controller

The number of test groups	Excitation frequency/Hz	Average picking time/s	Average rate of dropping flowers/%	Average rate of dropping fruits/%
19	12	94	3.7	93.2
20	12	97	3.1	92.6
21	12	93	4.6	94.4
22	15	91	5.7	93.1
23	15	94	5.1	90.2
24	15	95	4.9	87.2
25	18	86	5.7	88.2
26	18	88	5.4	95.6
27	18	91	5.5	96.7
Average		92.1	4.8	92.3